The four cumulus cloud modes and their progression during rainfall events: A C-band polarimetric radar perspective

Vickal V. Kumar,[1,2] Christian Jakob,[1,3] Alain Protat,[2] Peter T. May,[2] and Laura Davies[1]

[1]   There is no objective definition to separate cumulus congestus clouds from the shallow cumulus and deep clouds. This has generated misinterpretation about the role of congestus clouds to promote deep convection through the potential of moistening the middle troposphere. In this study, an objective identification for the different tropical cumulus modes is found by examining the occurrence frequency of the cloud cell top heights (CTHs) and near-ground (at 2.5 km height) rainfall properties of these cells using a three-season database of the Darwin C-band polarimetric radar. Four cumulus modes were identified, namely a shallow cumulus mode with CTH in the trade inversion layer (1–3 km), a congestus mode with tops in the highly stable middle troposphere (3–6.5 km), a deep convective mode with tops in the region of free convection (6.5–15 km), and an overshooting convection mode with tops in the tropical tropopause layer (CTH >15 km). The study also investigates the connections between these cumulus modes during heavy rainfall events. The congestus mode occurs predominantly from ~10 h prior to the peak rainfall event to ~2 h past the event. The deep cloud populations (Modes 3 and 4) have their maxima at and shortly after the time of the rainfall peak, with maximum occurrence just below the tropical tropopause layer. A comparison of the heavy rainfall events occurring in morning (oceanic) conditions against the afternoon (continental) conditions revealed a higher ratio of the shallow to the deep cloud population and a shorter transition time from the shallow to the onset of deep population in the morning-oceanic conditions than the afternoon-land conditions. It is also found through the analysis of the large-scale moisture budget data set that for both the morning and afternoon events, the moistening peaked before the peak in the congestus populations.

1.   Introduction

[2]   Progress in simulating clouds in general circulation models depends substantially on improvements in the cumulus cloud parameterizations and their coupling to boundary layer and cloud processes [*Jakob*, 2010]. Cumulus clouds have historically been thought of as primarily consisting of two modes: shallow cumulus, with cloud top heights near the trade inversion layer, 1–2 km above the surface, and deep cumulonimbus clouds, with cloud tops near the tropopause [*Malkus and Riehl*, 1964]. *Johnson et al.* [1999] provided observational evidence of a distinct third cumulus cloud mode, the midlevel cumulus congestus clouds, with cloud tops near the 0°C melting level. Because of their small cell size and their transitional nature from nonprecipitating to precipitating convection, it is relatively difficult to observe congestus clouds with remote sensors [e.g., *Miller et al.*, 1998; *Melnikov et al.*, 2011]. Yet, they have been implicated in playing an important role in the transition from shallow to deep convection through the potential of moistening the middle troposphere [e.g., *Kuang and Bretherton*, 2006; *Waite and Khouider*, 2010], although there is still some ambiguity if the moistening itself is vital to trigger deep convection [e.g., *Hohenegger and Stevens*, 2012]. It is the goal of this study to further investigate the role of congestus clouds in the transition from shallow to deep convection by providing an improved analysis of radar observations of this transition at Darwin, Australia, and by directly linking the radar observations to the large-scale dynamical state of the tropical atmosphere.

[1]School of Mathematical Sciences, Monash University, Melbourne, Victoria, Australia.
[2]Centre for Australian Weather and Climate Research, Australian Bureau of Meteorology and CSIRO, Melbourne, Victoria, Australia.
[3]ARC Centre of Excellence for Climate System Science, Monash University, Melbourne, Victoria, Australia.

Corresponding author: V. V. Kumar, Centre for Australian Weather and Climate Research, Australian Bureau of Meteorology and CSIRO, GPO Box 1289, Melbourne, Vic 3001, Australia. (v.kumar@bom.gov.au)

[3] There has been ongoing improvement in observing congestus clouds from radar observations with a focus on refining the criteria for their identification. Early studies identified congestus clouds as any precipitating convective cloud with cloud top heights (CTHs) between 5 and 9 km [*Johnson et al.*, 1999], while later studies included the criterion of the existence of a continuous radar echo from the near surface to the CTH [*Jensen and Del Genio*, 2006]. However, none of these studies provide a clear justification of choosing a 9 km CTH threshold. Early field campaigns, such as Global Atmospheric Research Program Atlantic Tropical Experiment [e.g., *Houze and Cheng*, 1977] and Tropical Ocean-Global Atmosphere Coupled Ocean-Atmosphere Response Experiment [e.g., *Rickenbach and Rutledge*, 1998], contained evidence of weak bimodality in cumulus occurrence. However, in these studies, cloud top peaks occurred near 2–3 and 6 km, with no evidence of a maximum at 9 km. Recent radar echo top analyses at Darwin using long-term data sets spanning several wet seasons showed limited support of multimodal distribution [e.g., *May and Ballinger*, 2007; *Kumar et al.*, 2013]. As there is still no agreed "definition" of congestus occurrence derived from radar observations, a first aim of this study is to develop a more objective identification of congestus and deep clouds. This will be achieved by a careful analysis not only of CTH occurrence frequency but also of the radar retrieved rainfall properties taking advantage of the polarimetric capabilities of the research radar deployed at Darwin (C-band polarimetric (CPOL) radar) [*Keenan et al.*, 1998].

[4] Once a method of identifying congestus and deep clouds has been established, a major motivation of this paper is to study the progression of different cumulus modes through the storm life cycle. Specifically, the goal here is to better comprehend the role of cumulus congestus clouds in preconditioning the atmosphere for deep convection. Several studies have found that the occurrence frequency of congestus clouds increases prior to peak rainfall events associated with deep convection [*Mapes et al.*, 2006; *Chen and Del Genio*, 2009; *Tromeur and Rossow*, 2010; *Del Genio et al.*, 2012]. *Kikuchi and Takayabu* [2004] performed a composite analysis of CTHs and thermodynamic profile as a function of the life cycle of the Madden-Julian oscillation, which revealed that the three cumulus cloud modes developed in stages. Initially, the weakening of the trade inversion layer corresponds to the shift from shallow cumulus to congestus cumulus. In the next stage, the cumulus congestus clouds moisten the atmosphere below the 0°C level, preconditioning the atmosphere for deep convection [*Kemball-Cook and Weare*, 2001; *Lin and Johnson*, 1996]. However, recently *Hohenegger and Stevens* [2012], using 1 month of satellite observations, found the transition time from congestus to deep convection to be much shorter (2 h over land and 4 h over the ocean) than the time needed (10 h and longer) for congestus clouds to sufficiently moisten the atmosphere. Their results do not support the idea that congestus moistening itself enhances the formation of deep convection. Rather, they suggested that dynamical processes, potentially related to the heating from congestus clouds, are likely an important ingredient in promoting the transition to deep convection. This study will further investigate this link by relating the observed cloud behavior to the large-scale state of the atmosphere around Darwin.

[5] In this paper, we use three wet seasons (573 days) of Darwin CPOL radar observations to investigate the statistical properties of cumulus congestus clouds, deep convective clouds, and overshooting convection, and their progression during rainfall events. In section 2 of this paper, the CPOL database is described. In this section, we also compare the CTH frequency derived from CPOL with concurrent CTH retrievals from a Darwin MilliMetre Cloud Radar (MMCR) [*Moran et al.*, 1998] to estimate the percentage of congestus clouds which could not be detected by the CPOL radar. Section 3 describes the statistical properties of the identified convective clouds as a function of CTH. This section will provide an objective method to identify cumulus modes, including congestus. Section 4 then focuses on the temporal evolution of the convective cell characteristics around heavy rain rate events to investigate the evolution of the cumulus modes throughout the storm life cycle. Section 5 investigates the potential connection of cloud growth to dynamical processes by analyzing moisture and heating tendencies around the rain events identified in section 4. We summarize our findings in section 6.

2. Data Sets and Method

2.1. The Darwin C-Band Polarimetric (CPOL) Radar

[6] The study primarily uses three wet seasons of data (October 2004–April 2005, October 2005–April 2006, and October 2006–April 2007) from the Darwin CPOL radar. The CPOL radar (12.25°S, 131.04°E) collects a three-dimensional volume of data out to a range of 150 km once every 10 min. Each volume consists of a series of 16 conical sweeps at elevations ranging from 0.5° to 42°. The radar transmits alternate linear horizontal and vertical polarization pulses, which give access to key polarimetric variables such as the horizontal reflectivity (Z_h), the differential reflectivity (Z_{dr}), and the specific differential phase (K_{dp}) [e.g., *Zrnić and Ryzhkov*, 1998].

[7] Next, the data are gridded by constructing a series of the constant altitude plan position indicator (CAPPI) at every 0.5 km in height (with a horizontal bin size of 2.5 km × 2.5 km) extending up to 20 km, using the Sorted Position Radar INTerpolation software. To minimize any issues that might occur during the interpolation from PPIs to CAPPIs, only data in the range 20–100 km and at heights greater than 2.5 km are analyzed. Furthermore, as the focus of this study is on the development of convective clouds in the transition from shallow to deep modes, the stratiform pixels are also excluded from the analysis.

[8] The individual radar pixels at a CAPPI level of 2.5 km are characterized as convective or stratiform using an algorithm by *Steiner et al.* [1995]. The Steiner algorithm classifies the gridded reflectivity as convective if the reflectivity value is at least 40 dBZ or greater than a fluctuating threshold depending on the area-averaged background reflectivity (within a radius of 11 km around the grid point). Each convective center has a radius of influence (ranging from 1 to 5 km) also depending on the surrounding background reflectivity [*Steiner et al.*, 1995]. This method of identifying the convective and stratiform radar pixels has been used in previous studies over the Darwin region [e.g., *May and Ballinger*, 2007; *Kumar et al.*, 2013; *Penide et al.*, 2013].

[9] All radar pixels in the vertical column above the altitude of 2.5 km are assigned the same Steiner classification as that at the 2.5 km CAPPI level. This assumption is reasonable since the vertical shear of horizontal wind between the heights of 2.5 and 12 km in convectively active Darwin wet season regimes is small, typically on the order of $10^{-4} \, \text{s}^{-1}$ [e.g., *Kumar et al.*, 2013]. Furthermore, as explained later, CTH values are calculated per cloud cell (i.e., several adjoining convective radar pixels) not per single vertical radar column. So the tilt of the convective core due to wind shear is expected to have a minimal effect on the cell-based CTH retrievals.

[10] From this gridded reflectivity data, CTH is calculated using the following two methods. First, the algorithm identifies convective cells occurring at the 2.5 km CAPPI level. Specifically, once a convective radar pixel is detected at 2.5 km height, the algorithm then searches in all directions in the horizontal plane from this convective pixel for any connected convective pixels and stops when no convective pixel is found (radar pixel classified as stratiform or clear air). The procedure is repeated in all directions, defining the contours of each convective cell. Some cells, typically those with low CTH, could have a sectional area of a size equal to one radar pixel with an area of $6.25 \, \text{km}^2$ ($2.5 \, \text{km} \times 2.5 \, \text{km}$). The next area size for two pixels is $12.5 \, \text{km}^2$ and so on. Second, for each identified convective cell, the maximum height of the 0 dB echo at any of the pixels in the cell is computed to provide an estimate of a single CTH for that convective cell. Specifically, the CTH corresponds to the radar echo height whose reflectivity is the closest to 0 dB, but with a reflectivity value within the range of -5 to $+5$ dB, and provided there is a vertically continuous reflectivity greater than 0 dB between the 2.5 km CAPPI level and this CTH. This procedure filtered out any possible effects of detached cloud layers situated above the convective towers.

[11] This definition of CTH is similar to the definition of an echo top height (ETH) used in previous studies [e.g., *Kumar et al.*, 2013], except that in those studies ETH was calculated for individual convective column instead of the whole convective cells used here. Using the common single-column ETH, a convective cell will have a distribution of ETHs and pixels from the same cell will potentially be classified in different cumulus cell categories, which complicates the use of this definition in studying the transition to deep convection. Using the same reasoning, the 0 dB height per cell is taken as the maximum height reached by any near-0 dB pixel in the cell, and not an average of all near-0 dB ETHs in that cell. In summary, throughout the paper, with the exception of Figure 1, one CTH per convective cell is used in the analysis. The reasons for the exception will be explained when introducing the figure.

[12] The choice of the 0 dB level as cell threshold is a compromise. The minimum detectable reflectivity (R_{min}) above the noise level as a function of CPOL range (R in km) is R_{min} (dB) $= -41.25 + 20 \log(R)$. *May and Ballinger* [2007] and *Kumar et al.* [2013] used 5 dB echo top height criteria mainly because they choose to use a large domain around the radar. Here, we use CPOL data only up to a range of 100 km ($R_{\text{min}} = -1.25$ dB), so the 0 dB threshold is sufficiently high to allow for detection of echoes at radar ranges considered in this study. The 0 dB top height criteria also ensure that the radar-determined CTH is even closer to the true CTH.
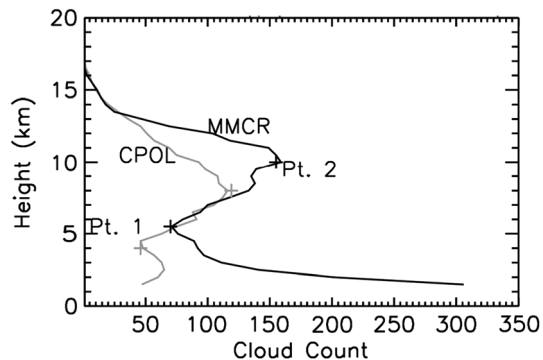

Figure 1. Distribution of cloud top height (CTH) occurrence frequency over the Darwin Atmospheric Radiation Measurement (ARM) site, 25 km from the Darwin C-band polarimetric (CPOL) radar center. The black and grey curves are the CTH frequency computed using the MilliMetre Cloud Radar (MMCR) and the range-height indicator (RHI) scan of CPOL, respectively. A bin size of 0.5 km in height is used in this figure and all subsequent figures.

[13] Apart from the CTH information per cell, we also make use of radar reflectivities, drop size distributions (DSD) parameters, and rain rate retrievals from the 2.5 km CAPPI level bounded by the respective convective cell area. As for CTH, we define only one value per cell rather than using individual pixel values. This is done by calculating the cell mean reflectivity, rain rate, drop size diameter (D_0), and number concentration of small hydrometers (N_w) at each vertical level. Descriptions of the algorithm used to retrieve drop size distributions (DSD) parameters and rain rates from the polarimetric radar variables are given in *Bringi et al.* [2009]. It assumes a normalized gamma DSD form [*Testud et al.*, 2001] described by the median volume diameter (D_0) and the "generalized" intercept parameter (N_w). For simplicity, N_w can be thought as the number concentration of small hydrometers. N_w is the same as the intercept parameter of an exponential DSD with the same D_0 and liquid water content as the gamma DSD. This algorithm uses a multiparameter approach to take advantage of the complementary information contained in the polarized backscattered signals. First, D_0 is retrieved from the differential reflectivity using polynomial fits (e.g., $D_0 = f(Z_{dr})$), then N_w is estimated using a power law of the form $Z_h/N_w = c.(D_0)^d$, and finally, the rain rate is estimated using either a function of the form $R = f(K_{dp})$, $R = f(Z_h, Z_{dr})$, or $R = f(Z_h)$ depending on various thresholds and a decision tree [*Bringi et al.*, 2009].

2.2. Cloud Radar Data and its Comparison to CPOL

[14] A major objective of this paper is to study the features of cumulus congestus clouds. These clouds have been typically studied using data from a millimeter-wavelength MMCR, except in *Johnson et al.* [1999], where C-band radar measurements were used. Millimeter-wavelength radar has been preferred to study congestus clouds because some of the clouds in this mode could be nonprecipitating and thus will be missed by a centimeter-wavelength radar. Darwin hosts both a vertically pointing MMCR with a wavelength of 8.6 mm [*Moran et al.*, 1998] at the U.S. Department of Energy's Atmospheric Radiation Measurement (ARM)

[Stokes and Schwartz, 1994; Ackerman and Stokes, 2003] site and the scanning CPOL (5.3 cm) operating over the wet season, thus offering the potential of estimating the congestus cloud fraction which will be missed by the C-band radar.

[15] The best way to achieve a reasonable space-time overlap between the vertically pointing MMCR and scanning CPOL radars is to use the data from the range-height indicator (RHI) scanning mode of the CPOL radar. CPOL performs RHI scans over the MMCR site lasting for approximately 10 s using 70 different elevations ranging from 0.02° to 45.8°, once every 10 min. Thus, RHI scans have a much finer vertical resolution (10 m near the surface and ~15 m at maximum elevation) than the PPI mode, which uses 16 elevations and has a vertical resolution on the order of few hundreds of meters. The RHI scanning routine on CPOL commenced only in October 2005; only 2 years of statistics is used in the comparison of the two radar results.

[16] The reflectivity data from the RHI scans are averaged over three adjacent range gates centered on the MMCR site (25 km) [e.g., Bringi et al., 2009]. Then, height profiles are constructed using the radar beams at the 70 different elevation angles. In comparison, the MMCR radar does a continuous vertical sounding with a temporal resolution of 35 s and a fixed height resolution of 90 m. We time-match the two radars by selecting only the MMCR scans closest to the RHI scan times. RHI scans which had no echo detection at the MMCR location, and vice versa, were still kept to build the time-matched array. Apart from inevitable instruments problems, it is fair to assume that both radars over the time-matched interval observe the same type of clouds. Next, the column ETH is computed using the reflectivity profiles from both radars, using the same criteria defined in Jensen and Del Genio [2006]. Specifically, ETH is computed as the maximum height reached by the radar echo, provided there is a continuous echo from cloud base to the ETH. Note that the starting cloud base height for both radars is required to be less than 2 km. Because of this requirement, the cloud data used in this analysis are likely mainly convective in nature [e.g., Jensen and Del Genio, 2006]. At the ETH, the CPOL reflectivity is required to reach 0 dB, but for the MMCR, the reflectivity at the ETH is set to the lowest available reflectivity per column, which was typically ~ -20 dB. Even though the minimum reflectivity that could be measured by CPOL at the range of 25 km is $R_{min} = -13$ dB, well below the 0 dB ETH requirement, 0 dB ETHs are preferred so that the radar comparison remains relevant for all CPOL ranges (20–100 km) used in the rest of this study.

[17] Figure 1 shows the cloud count from MMCR (black) and CPOL RHI (grey) radars in CTH bins of 0.5 km. There are several interesting similarities and differences in the two CTH profiles. As one would expect, the MMCR detects significantly more clouds below 4 km, owing to its ability to see nonprecipitating cloud particles. Above 8 km the top heights from the CPOL radar are approximately 2 km lower than those obtained from the MMCR. Again, this is likely because the MMCR can detect much lower reflectivities (the modal reflectivity value is near −20 dB), whereas the CPOL reflectivities at the ETH are set to be 0 dB. So the true cloud top height for deep clouds is likely within 2 km of the 0 dB CTH of CPOL, consistent with those estimated by previous studies [e.g., Kingsmill and Wakimoto, 1991;

Casey et al., 2012]. Interestingly, in the range of congestus cloud top heights between 4 and 8 km, the radars agree well.

[18] Overall, CPOL detects 67% of the clouds detected by MMCR; most of the missing clouds are in the shallow cumulus mode below 4 km. At the heights of 4 and 8 km, the ratio of CPOL detection to MMCR detection is 50% and 82%, respectively. However, such direct comparison for a given height is thought to be less useful due to the difference in the sensitivity of the two radars. Instead, we estimate the CPOL efficiency using the following procedure. The first local minimum (Pt. 1, 4.0 km in CPOL and 5.5 km MMCR) in both curves is assumed to be the breakpoint height of the shallow clouds, and comparing the total cloud counts below this level from both radars gives a detection efficiency of 30% on CPOL compared to MMCR. Similarly between Pt. 1 and Pt. 2 (possibly the congestus fractions), the CPOL efficiency is 64%, and above Pt. 2 it is 127%. The CPOL radar detects more of the deeper clouds compared to MMCR since the millimeter-wavelength signals are often attenuated during periods of moderate and heavy rain rates associated with deep clouds [e.g., Kumar and Ramachandran, 2004].

2.3. The Large-Scale Atmospheric State

[19] It is a goal of this study to connect the cloud evolution in the transition from shallow to deep convection to the dynamical evolution of the large-scale atmospheric state. To do so, we require reliable estimates of the large-scale state concurrent with the radar observations. Jakob et al. [2011] have derived such a data set for the Darwin region for the same wet seasons for which radar observations are available in this study.

[20] The data set is constructed by applying the variational budget analysis algorithm of Zhang and Lin [1997]. This algorithm usually requires an array of atmospheric sounding data, as well as observations of surface precipitation and top of the atmosphere radiation, to optimally estimate all terms of the vertically resolved heat, moisture, and momentum budgets. In the absence of a radiosonde array, Xie et al. [2004] proposed to use results of numerical weather prediction analyses as a surrogate. To test this approach in the Darwin region, Jakob et al. [2011] applied this approach to the Tropical Warm Pool International Cloud Experiment [May et al., 2008] data set and showed that the use of soundings extracted from the operational analyses of the European Centre for Medium-Range Weather Forecasts provided a very close approximation to budget estimates using a full sounding array. They then applied the method to three full seasons of data using surface precipitation rainfall, calculated from the CPOL radar as a key constraint to the moisture budget. The resulting large-scale data set used here includes vertical profiles of heat and moisture budgets as well as thermodynamic and dynamic variables at 40 hPa vertical and 6 h temporal resolution. The spatial domain of the large-scale data set is shown in Xie et al. [2010] and is comparable to the CPOL domain with a radius of 100 km.

3. The Statistical Rain Properties of Individual Convective Cells

[21] In this section, the CPOL observations are used to study in detail the near-surface (at a fixed height of 2.5 km) characteristics of two of the three cumulus cloud modes

identified in *Johnson et al.* [1999]: congestus and deep clouds. As will be shown, the deep cloud mode is found to comprise two distinct types of cloud with very different properties. The shallow cumulus mode cannot be included here because many shallow cumulus clouds do not produce sufficiently large droplets to be detected by the C-band radar (cf. Figure 1). Another limitation is that at the maximum range of the radar used here (100 km), the first conical scan of elevation 0.5° has a minimum detection height of 1 km, hence missing the very shallow cumulus clouds forming at further ranges.

[22] A total of 640,419 convective cells were identified over the three seasons, and their frequency of occurrence in 0.5 km bins of CTH is shown Figure 2a. An overall occurrence peak is evident at 7 km, with no clear evidence of a distinct third peak associated with the deep clouds. Instead, there is a near-constant reduction in the number of clouds with CTH. Thus, at face value, there is limited evidence supporting the cumulus trimodality theory [e.g., *May and Ballinger*, 2007; *Kumar et al.*, 2013]. Note that in our data set, a third occurrence peak associated with deep clouds becomes noticeable on many afternoons associated with sea breeze convergence [*Kumar et al.*, 2013] and during heavy rainfall events (see below).

[23] Instead of focusing purely on numbers, we investigate the convective rainfall properties as a function of CTH. The solid lines in Figures 2b and 2c, respectively, show the mean cell area and convective area fractions at 2.5 km height as a function of CTH. Convective area fraction is the ratio of the total area covered by all convective cells belonging to a certain CTH bin divided by overall total convective area. Hence, the area fraction response is proportional to the product of mean cell area (solid line in Figure 2b) and total number of cells (Figure 2a). Thus, it follows from here that the increase in convective area fraction below 7 km is mainly due to the rapid increase in the number of cells (Figure 2a), since the mean cell area is constant for these cumulus congestus clouds. In contrast, the convective area fraction with cells with CTH between 7 and 13 km is remarkably constant. This is because even though the cell numbers reduce with increasing CTH in this region (Figure 2a), their cross-sectional area at 2.5 km height grows wider as they become taller (solid line in Figure 2b). The deepest convective cells (CTH > 13 km) have the largest convective area fraction, though only 1% higher than that from clouds with a CTH between 7 and 13 km. This largest contribution of deeper convective clouds is linked to a rapid increase in the mean horizontal area of cells (solid line in Figure 2b) with CTH > 13 km (Figure 2a).

[24] The convective rain accumulation fractions (dotted line in Figure 2c) increase almost linearly with increasing CTH up to a CTH of 17 km. This parameter is the ratio of the total rain accumulation associated with a given CTH bin divided by overall total convective rainfall. The rain accumulation fraction response is related to the product of the number of convective cells (Figure 2a), mean cell area (solid line in Figure 2b), and the mean cell rain intensity (dotted line in Figure 2b). Thus, the almost linear behavior in convective rain accumulation fraction is caused by two of the three controlling variables, the cell raining area and cell rain intensity, both of which increase somewhat exponentially with CTH.
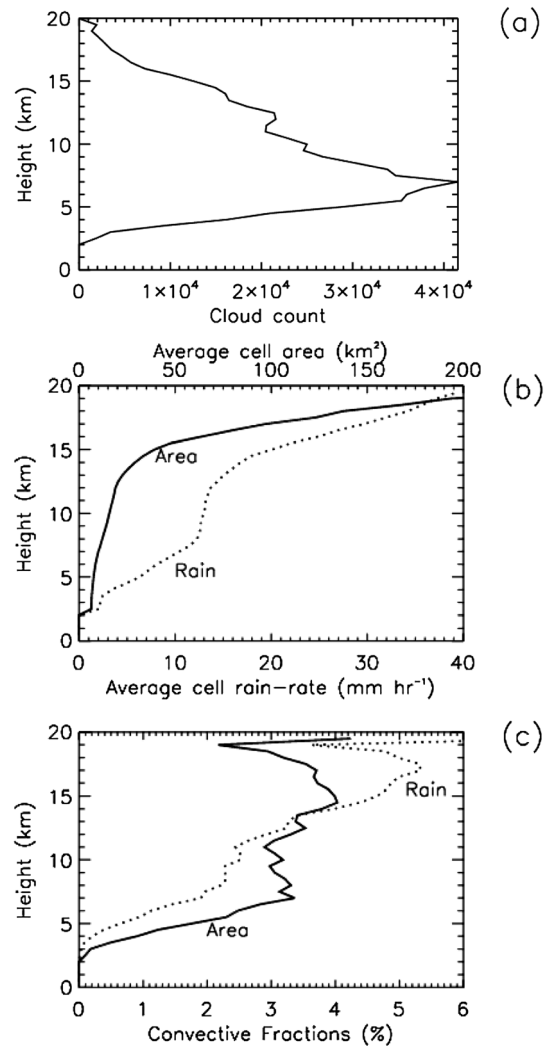

Figure 2. (a) The same format as Figure 1 except the CTH is computed using gridded (CAPPI) CPOL data. (b) Average cell area (solid) and cell rain rate (dotted) using data from 2.5 km CAPPI levels bounded by the convective cell area, as a function of CTH. (c) The same format as Figure 2b and shows the fraction (total at a given CTH divided by overall convective total) contributed by each CTH bin.

[25] The behavior of mean cell rain intensity as a function of CTH (dotted line in Figure 2b) perhaps reveals the most convincing evidence of the different cumulus categories. Specifically, the rain intensity at 2.5 km increases at a rate of 1.9 mm h^{-1} km^{-1} with increasing CTH when CTH is below 7 km. It increases at the much lower rate of 0.4 mm h^{-1} km^{-1} when CTH is between the 7 and 15 km, and then again displays a very large increase at a rate of 4.3 mm h^{-1} km^{-1} when CTH is above 15 km. This behavior is intriguing, suggesting the possibility of three (instead of the usual two) modes of precipitating convection in addition to the shallow mode (undetectable in this study). This hypothesis is further explored below using the radar reflectivity and all DSD parameters.

[26] Figure 3 shows the probability distribution function (PDF) of radar reflectivity at 2.5 km in 0.5 km bins of CTH.
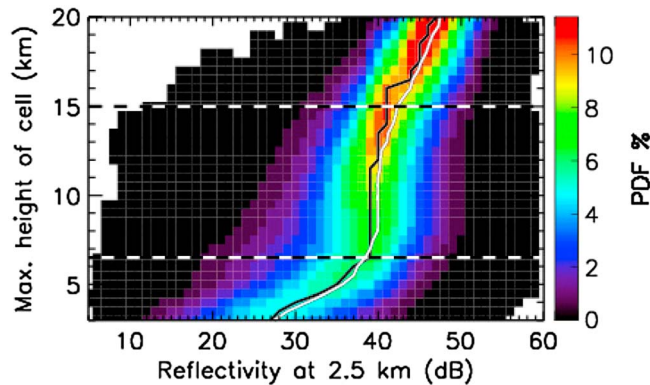
Figure 3. PDF of reflectivity using a bin size of 1 dB and as a function of CTH. One mean reflectivity was obtained per convective cell using reflectivity pixels that are bounded by the respective convective cells at the 2.5 km CAPPI level. The white curve is the overall mean reflectivity at each CTH level, and the black curve is the modal reflectivity. The dashed horizontal lines correspond to the breakpoints in the reflectivity trend indicating the lower (6.5 km) and the upper (15 km) CTH boundary for the "normal deep convection."

Recall from section 2 that each cell is assigned one reflectivity value, which is the mean of the radar reflectivity pixels from the 2.5 km CAPPI level belonging to that cell. The evolution of the 2.5 km reflectivity distributions with CTH clearly indicates the presence of two separate inflection levels: one at 6.5 km and another at 15 km (marked by horizontal lines). Cells with CTH below 6.5 km have a broad distribution in reflectivity at 2.5 km height with the smallest modal (black curve) and mean (white curve) reflectivities of all CTH classes. With increasing CTH, the reflectivity distribution at 2.5 km height becomes narrower with the mode-mean reflectivity values strongly increasing. The broad distribution in reflectivity PDFs in cells with lower CTH is thought to be because it is made of a mixture of nongrowing terminal congestus clouds with mainly lower reflectivities and growing transient congestus cloud with predominantly higher reflectivities. This hypothesis is being further explored in a separate study. When cell CTH is between 6.5 and 15 km, the 2.5 km reflectivity distribution is nearly constant with some narrowing with CTH evident. The modal and mean reflectivities are both around 38 dBZ, though the lower reflectivity cells do become also frequent with increasing CTH. In contrast, above 15 km the response in reflectivity with increasing CTH is similar to cells with CTH below 6.5 km, except that the distributions are much narrower and have much higher modal and mean reflectivities.

[27] Figures 1–3 together with the three-season average temperature lapse rates (Figure 4) support the existence of four different cumulus cloud modes:

[28] 1. Mode 1 (not studied here) consists of shallow cumulus clouds and is the most dominant cloud type. The CTHs of these clouds are in the trade inversion layer (1–3 km), which had a high static stability of the lapse rate ranging from −6 to −5 K km^{-1}.

[29] 2. Mode 2 represents the congestus cloud category, and the CTH of these clouds is between 3 and 6.5 km. Its minimum boundary height of 3 km is marked by an increase in midlevel stability, which reached the maximum stability at the melting level (ML) of 5 km. The relative humidity also increases from 3 km to the ML and from thereon decreased steadily with height (not shown).

[30] 3. Mode 3 is denoted as the "normal" deep convective cloud mode with top heights between 6.5 km and the level of zero clear-sky radiative heating (~15 km).

[31] 4. Mode 4 represents overshooting deep convection and with tops in the tropical tropopause layer (TTL; CTH >15 km). As these clouds penetrate through the strongly stable tropopause, they represent the most vigorous convection, as indicated by their high reflectivity at 2.5 km.

[32] We continue the investigation of the hypothesized modes of convection by exploring the distributions of rain rate and key DSD parameter retrievals at 2.5 km in the same manner as the reflectivity. Figure 5 shows the distributions of cell rain rate, D_0, and N_w at 2.5 km confirming the existence
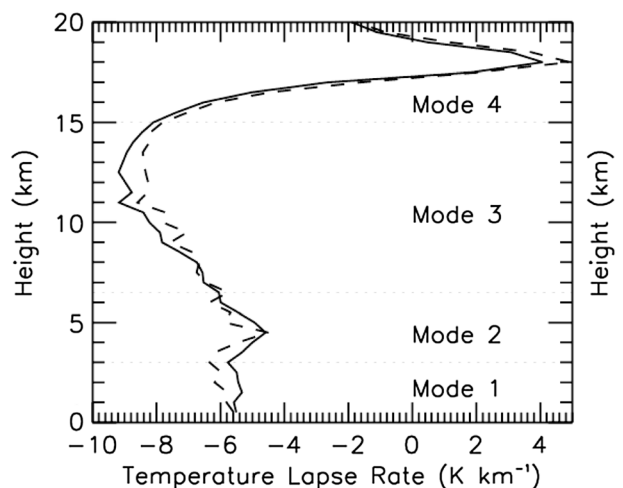

Figure 4. Average (solid) and median (dashed) temperature lapse rates associated with the convective cells. Prior to data processing, each convective cell is tagged with the nearest radiosonde profile, provided the sounding is within ±3 h of the convective cell identification time. Thus, an individual sounding profile may be used several times and some convective cells had no sounding data. The significances of Modes 1–4 have been explained in the text.
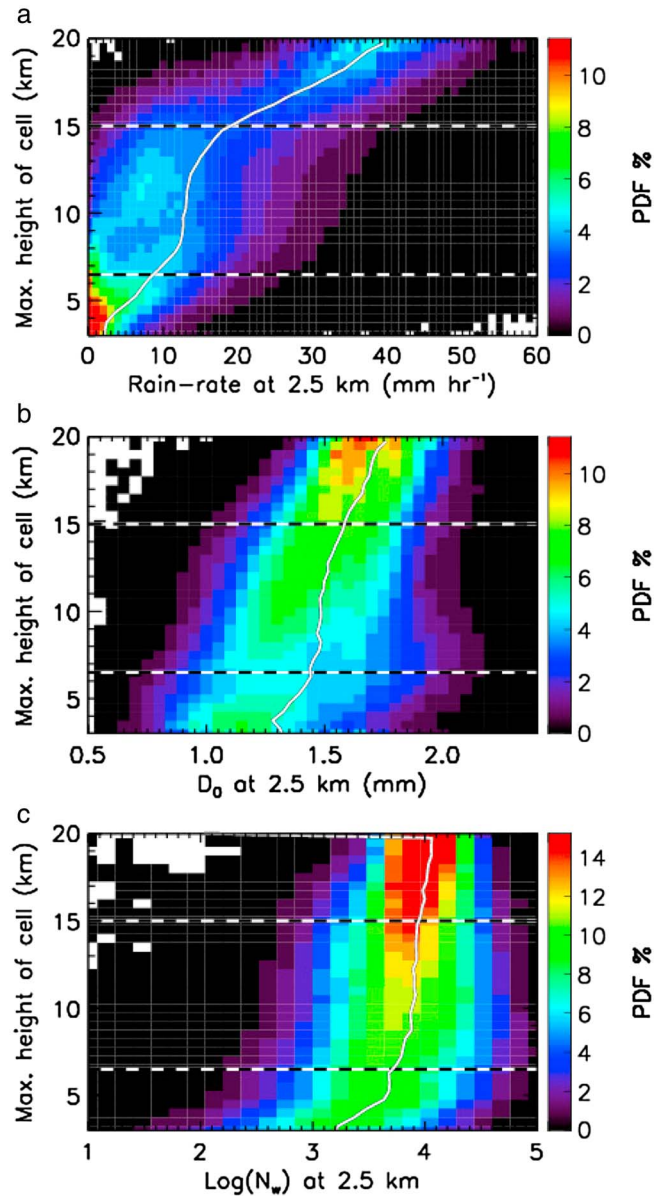
Figure 5. The same format as Figure 3 and shows PDF of (a) rain rate using a bin size of 1 mm h^{-1}, (b) D_0 using a bin size of 0.05 mm, and (c) log$_{10}$(N_w) using a bin size of 0.15. The white curve is the overall mean of the rainfall properties in each CTH bin.

of the three precipitating cumulus modes proposed earlier. The congestus mode displays strongly positively skewed rain rates at 2.5 km height, with the mean rain rate increasing as the cells grow higher (Figure 5a). They also typically have a small median volume diameter (D_0) and small concentrations of small hydrometeors (N_w) at 2.5 km height compared to the other two deeper cloud modes. The deep convective mode had the largest range in rain rate distribution at 2.5 km height. However, as is the case with reflectivity, the rate of increase in rain rate with increasing CTH is small. For the overshooting mode, the rain rate and DSD parameter distributions at 2.5 km height are narrow. The mean rain rate increased steeply as the cells grow taller into the TTL layer. Another notable observation is that rain rates of intensity greater than 30 mm h^{-1} occurred almost exclusively with

Mode 4, highlighting the potential importance of this mode for extreme convective rainfall.

[33] Having focused on the 2.5 km only so far, next we investigate vertical profiles of reflectivity for different CTH classes by calculating the reflectivity lapse rate for some selected CTH levels (Figure 6a). The reflectivity lapse rate is defined as the vertical gradient of reflectivity [e.g., *Zipser and Lutz*, 1994]. Recall from our method of calculating CTH, the maximum reflectivity value at the top of the cell will be near 0 dB. Also, to aid the discussion, the relative humidity profiles associated with the different CTH classes are shown in Figure 6b. Again, even the vertical profile of reflectivity (Figure 6a) clearly shows the presence of the three separate precipitating cumulus cloud modes. The congestus mode (black and grey in Figure 6a) has the largest reflectivity lapse rate of approximately 7 dB km^{-1}. A broad
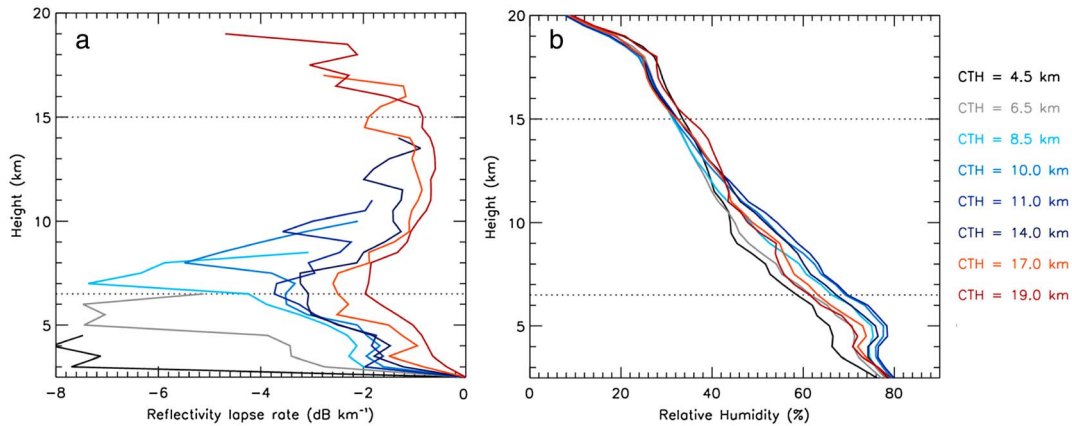
Figure 6. (a) Vertical profile of reflectivity lapse rate (defined as vertical gradient of reflectivity) within the convective cloud from the altitude of 2.5 km to CTH. The lines represent the lapse rates for selected CTH types. (b) Vertical profile of relative humidity associated with clouds in each CTH bin. The sounding profiles are selected in the same manner as temperature lapse rates in Figure 4. Note that an individual sounding profile is attributed to several different CTH types occurring within the 6 h window. However, by calculating a mean profile of several thousand cases of a particular CTH type, the underlying signature will likely be revealed.

peak in lapse rate occurs in the region from roughly 1.5 km below the CTH to CTH. In contrast, cells in the deep convective mode (light blue-dark blue) have a much narrower peak in lapse rate at ~1.5 km below the CTH and a second peak of approximately 3.5 dB km^{-1} occurs near the ML. The overshooting deep convective mode (light red-dark red) also had a maximum at the ML and then lapse rate increased steadily in the TTL. Overall, all CTH classes seem to suffer a large loss in vertical momentum as they penetrate past the highly stable "ML lid." The consistent peak in lapse rate at ~1.5 km below the CTH, which for Mode 2 clouds and shallow clouds in Mode 3 is mixed with the ML peak, is an indication that the vertical momentum of cumulus cells is reducing rather abruptly as the convective mass flux detrains into stratiform anvils as they approach their equilibrium heights.

[34] It is clear that the maximum reflectivity lapse rate is the largest in cells with lower CTH and this amplitude decreased gradually with increasing CTHs. This result is likely a direct consequence of weaker vertical velocities in shallow cells compared to deep convective cells [e.g., *Zipser and Lutz*, 1994]. However, the atmosphere is found to be drier when there are shallow cells (Figure 6b), and dry air entrainment into clouds will also limit the vertical extent of convection [e.g., *Redelsperger et al.*, 2002]. Similar arguments can be made about deep and overshooting convection; they are growing higher because they either have strong updraft speed and/or the middle atmosphere is moist. Interestingly, it is the Mode 3 "weaker" deep convection that occurs in the highest relative humidity, while the stronger Mode 4 convection occurs at intermediate relative humidity, indicating that the relationship between the depth of convection and middle tropospheric humidity is far from simple. Of course, this relationship is potentially affected by the coarse temporal and spatial resolution of radiosounding data. It is well known that strong convection in the Darwin area occurs near coastlines and over islands [e.g., *Schafer et al.*, 2001] and processes associated with the development of convection

in complex terrain are likely factors in determining the CTH. We will investigate this further in the following section.

4. The Life Cycle of Convective Rainfall Events

[35] The characteristics of convective clouds during heavy rainfall events (hereafter referred as storms) are known to depend on a number of variables, such as the large-scale atmospheric state, local time, the underlying surface type, and internal storm dynamics [e.g., *Simpson et al.*, 1993; *Pope et al.*, 2009b; *May et al.*, 2012; *Kumar et al.*, 2013]. In this section, a composite method is used to identify peak convective rainfall events and to examine variations in convective cell characteristics several hours prior and after the peak rainfall time. This will provide some insights into the evolution of the convective modes identified in section 3 around main rainfall events including insights into the transition from shallow to deep convection.

4.1. Heavy Rainfall Events and Their Temporal Evolution

[36] To identify isolated heavy rainfall events in the CPOL data, two selection filters operating in sequence were used here. The first pass includes the computation of the 10 min domain-mean convective rain rate (DMCR) using data at the 2.5 km CAPPI level over the three seasons. Specifically, the DMCR is the sum of rainfall at all convective rain pixels (2.5 km × 2.5 km) divided by the constant radar coverage area of 43,982 km^2. The hourly running average DMCR values are calculated using the 10 min radar measurements, and this is done to remove short-timescale variations in DMCR. Rainfall events are then found by requiring the hourly running average DMCR peak to be larger than the three-season median DMCR of value 0.05 mm h^{-1}, and DMCR values to decrease on either side of this peak. Once each peak is identified, the hourly running average DMCR values on either side of the peak are scanned to determine the local minima. The local minima must be below the three-season
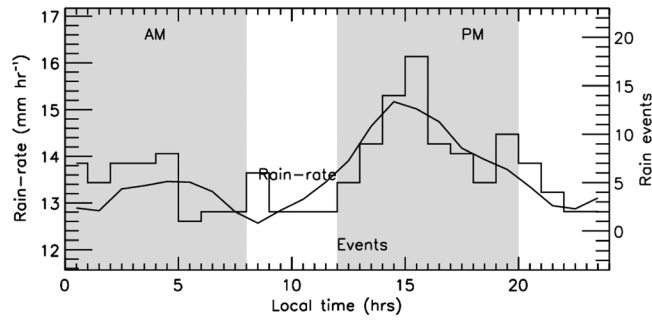
Figure 7. Diurnal variation of radar rain rate (curve) and count of identified rain events (line). The shaded grey region highlights our AM (00:00 A.M.–08:00 A.M.) and PM (12:00 P.M.–08:00 P.M.). These local time intervals are analyzed separately in the subsequent figures.

median DMCR and must be at least 1 h in time away from the peak DMCR. This way all events will have a lifetime of at least 2 h. As our focus is on the transition from shallow to deep convection, it was also ensured that only the first peak from multipeak rain events was selected for the analysis. A total of 371 events were selected using this first pass.

[37] The second pass keeps only those events that fall in the heavy rainfall category determined using the 6-hourly CPOL domain mean rain rate. Note that the 6-hourly domain mean rain rates were calculated using both stratiform and convective 10 min radar rain rate data. The lower limit of the heavy rainfall category is found to be $\sim 0.4\,\mathrm{mm\,h^{-1}}$, which corresponds to the upper tercile of the 6-hourly domain mean rain rates after periods without rain are excluded.

[38] This second pass just keeps 144 events from the initial total of 371 events, and the histogram of the diurnal variation of this final set of events is shown in Figure 7 (line). Also shown in this figure is the three-season average convective rain intensity (curve). The rain intensity response is reminiscent of the typical tropical maritime continent climate, with a strong afternoon and weak morning peak associated with land and oceanic underlying surface types, respectively [e.g., *Liu and Zipser*, 2008]. The histogram of the storm events also follows the rain intensity variation, with a dominant occurrence peak in the afternoon.

[39] Figure 7 confirms that rainfall in Darwin, when averaged over long times, shows a semidiurnal variations often associated with the underlying surface [e.g., *Kumar et al.*, 2013; *May et al.*, 2012]. For this reason, the convective cell characteristics during the rainfall events will be studied separately for the two broad local time categories: 00:00 A.M.–08:00 A.M. (hereafter AM class with 39 events) and 12:00 P.M.–08:00 P.M. (hereafter PM class with 78 events). The spatial distribution of convective rain intensity for these events is calculated using radar data from within 1 h on either side of the peak rainfall events and is shown in Figure 8. It is evident that the AM and the PM class strongly separate by the location of the highest rain intensity over ocean and land, respectively. We also find that nearly 60% of rainfall events in the PM class and 40% of events in the AM class occur in the most commonly observed moist easterly regime associated with the buildup and retreat of the Australian monsoon as well as monsoon breaks [*Pope et al.*, 2009a; *Kumar et al.*, 2013]. The second highest occurrence (nearly 30%) of rainfall events in the AM class is during the deep westerly "monsoon" regime and that in the PM class is in the shallow westerly regime, both of which are typical for monsoon conditions.

4.2. The Composite Life Cycle of Convective Cell Properties

[40] Figure 9 shows the results of a composite analysis of the radar data 12 h on either side of each peak DMCR event. The DMCR amounts are shown in Figure 9a. Figure 9b shows some of the components that constitute the DMCR including the total number of convective cells (black), the
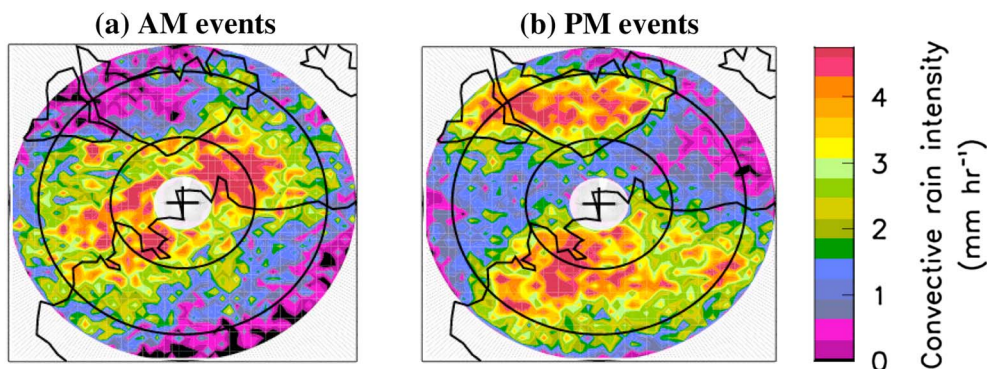
(a) AM events   (b) PM events

Figure 8. Spatial map of mean convective rain intensity within 1 h on either side of convective rain events that were identified to occur within (a) 00:00 A.M.–08:00 A.M. and (b) 12:00 P.M.–08:00 P.M. The concentric rings are 50 km apart.
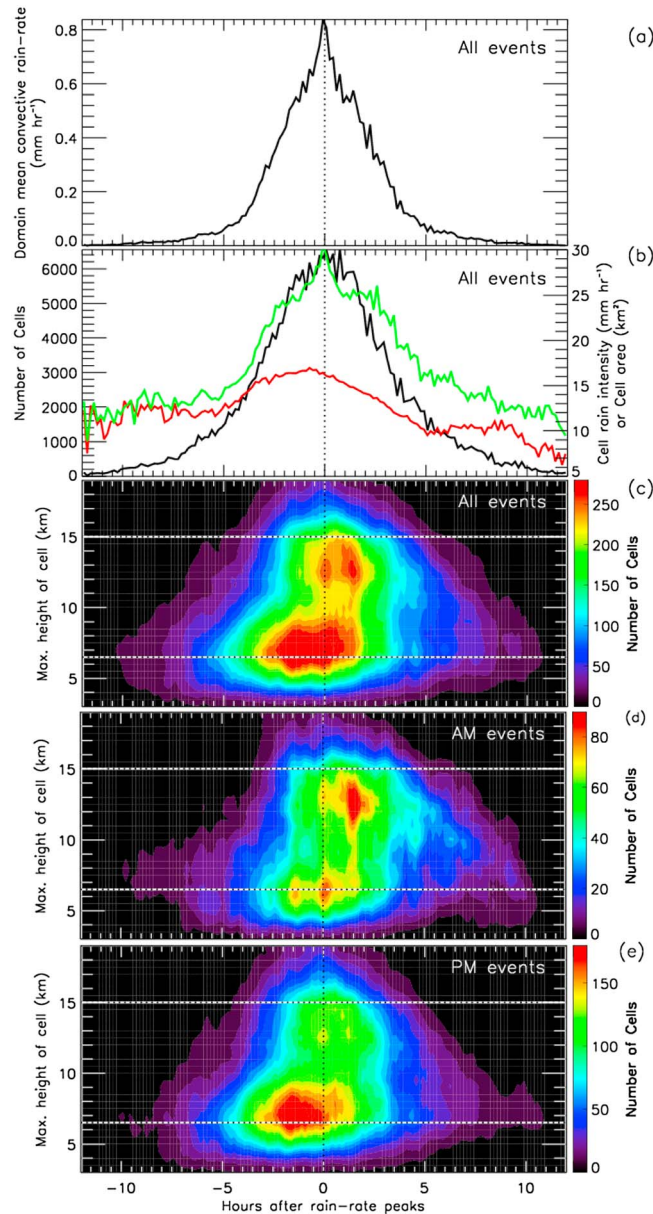
Figure 9. Composite responses of CTH for up to 12 h on either side of convective rain accumulation peaks to define controls (*t* = 0). A bin size of 10 min in time was used in this figure. (a) Composite of the 10 min domain average convective rain rate. (b) Composite of the total number of cells (black), average rain intensity (red), and average convective cloud area (green). (c) Composite of cloud top counts using a bin size of 0.5 km in height. (d and e) The same as Figure 9c except only using control times which are within AM and PM periods, respectively.

average cell area at 2.5 km (green), and the average cell rain rate (red). Figures 9a–9c show the results using all rainfall events (144 in total), while Figures 9d and 9e show the AM (39 events) and PM (78 events) classes separately.

[41] As is evident from Figure 9b, rainfall events start with a small number of small cells of medium intensity approximately 10 h before the peak in DMCR. From thereon, the cell number steadily increases up to its peak coincident with the DMCR peak. In contrast, cell size and intensity remain constant until a distinct increase roughly 5 h before the peak. Rain intensity peaks about 1 h before the DMCR peak, while cell size continues to grow peaking at the same time as DMCR. In other words, it is the rain area (determined by both

the number and size of the cells) that determines the timing of the rainfall peak, not the rain intensity. This feature is most clearly defined in the PM class (not shown) with a lag time of 40 min between the intensity and DMCR peaks.

[42] Figure 9c shows the distribution of CTH in bins of 0.5 km and as a function of storm time. Figure 9c reveals two dominant cell populations. The first of these has CTH from 5 to 8 km (Mode 2), while the second shows CTH between 10 and 15 km (Mode 3) and, while less frequent, evidence of overshooting convection (Mode 4). Cell counts for Mode 1 (not shown because CPOL does not detect most of the shallow cumulus clouds) actually peaked shortly before the peak in Mode 2 and remained higher throughout
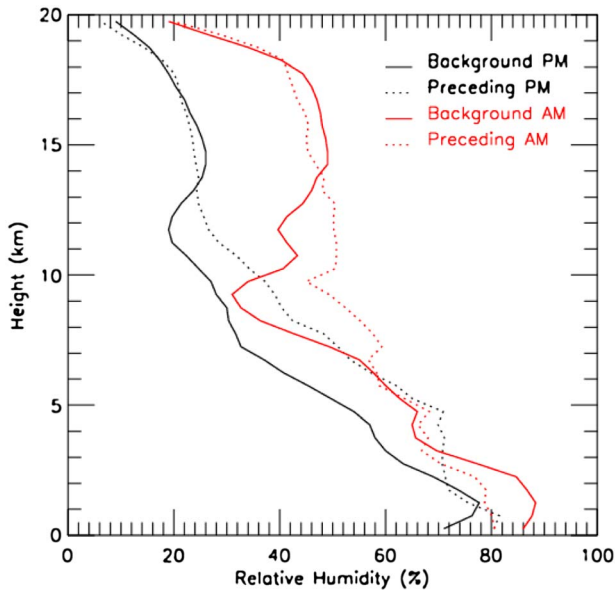
Figure 10. Mean vertical profile of relative humidity using radiosounding data during the interval 0–6 h preceding the onset of the 39 AM events (dashed red curve) and 78 PM events (dashed black curve). The solid red and black curves are background mean profiles obtained using all the 3 year radiosounding profiles between 00:00 A.M.–08:00 A.M. and 12:00 P.M.–08:00 P.M., respectively.

the heavy raining time. The shallower cloud population (Mode 2) occurs predominantly (more than 100 cells per bin) from ~8–10 h prior to the peak rainfall event to ~2 h after the event, with its peak frequency leading the peak rainfall by about 2 h. One notable feature in Figure 9c is that the increase in cell size and intensity noticed above coincides with a rapid growth in cloud depth about 5 h before the DMCR peak. The deep cloud population (Modes 3 and 4) has a maximum occurrence just below the TTL and maxima at and shortly after the time of the rainfall peak. The onset time of the deep cloud population lags that of the shallower one by 4 h, with a more uniform decay of both deep and shallow clouds 2–3 h after the peak rainfall. From the above results, we can identify roughly three stages of the storm development—a buildup phase (~5–10 h before the peak rainfall), a mature phase (5 h before to 1 h after the peak), and a decay phase (from 1 h after the rainfall peak).

[43] The distribution of CTH in the PM class (Figure 9e) is mostly similar to that observed in Figure 9c (all 144 events), since the PM class had 54% of rainfall events (see Figure 7). Notable features in the AM class (Figure 9d) which are somewhat different when compared to all events (Figure 9c) and PM statistics (Figure 9e) included the following: the ratio of the deep to the shallow population is higher (80% versus 30% in the PM class) and the lag time between the onset of the shallow to the onset of the deep population appears to be shorter. Also, the mode heights of the two dominant cell populations are lower in the AM class than in the PM class, and there are relatively less overshooting deep convective cells in the AM class.

[44] It seems intuitively consistent that in the AM class (oceanic) there is a faster transition time and higher deep to shallow cloud cell population ratios than for the PM class (continental) since the atmospheric moisture content is expected to be higher over ocean than land. Figure 10 shows that in the hours preceding the onset of heavy rainfall events in both classes, the relative humidity is higher in the middle troposphere (6–14 km; dotted lines in Figure 10) than in the background averages (solid lines). The feature of higher midlevel tropospheric moisture preceding deep convection has been documented in several studies [e.g., *Sherwood and Wahrlich*, 1999; *Mapes et al.*, 2006]. It is also evident from Figure 10 that the relative humidity associated with the AM events is higher in the middle troposphere, ranging between 50% and 60%, compared to that with the PM events with means between 25% and 50%. The presence of more moisture in the middle troposphere preceding the AM events compared to PM events will allow deep convection to form rather easily and quickly after shallow convection. An important question is what the source of this moistening preceding the onset of deep convection in both classes is. This will be further explored in section 5.

[45] Next, we explore the associated composite life cycle of convective cell microphysics around the rainfall peak using rain rate, mean drop diameter D_0, and drop concentration N_w retrieved at the 2.5 km CAPPI level from the dual-polarization radar observations (Figure 11). The objective here is to investigate the role played by convective-scale microphysics in the temporal evolution of rainfall over the composite life cycle shown in Figure 9, as well as in differences between AM and PM events. The "all events" plot is not shown, as it exhibits features very similar to the PM class (Figure 11, right). To help with the interpretation, we also show selected contours of normalized CTH occurrence frequency (black curves) from Figures 9d (AM class) and 9e (PM class). Note that the total CTH count is divided by the number of events in each class.

[46] Looking at Figure 11 (right), it appears clearly that the three main steps identified for the life cycle of convective cloud tops are all associated with major changes in convective-scale microphysics. In the buildup phase (~5–10 h before the peak rainfall), the D_0 and N_w at 2.5 km progressively increase as cloud top height increases over time, from about $D_0 = 1.2$ mm (and $\log10(N_w) = 3.8$) at $t = -10$ h for shallow congestus cloud top heights (below 7 km) to $D_0 = 1.6$ mm (and $\log10(N_w) = 4.3$) at $t = -5$ h for deep convective cloud tops reaching 10 km. The AM events (Figure 11, left) results are very different in that buildup phase, which are characterized by a large decrease in D_0 associated with deep convective cloud tops reaching 7 to 12 km (unlike the PM events) and an increase in mean N_w (like the PM events). Interestingly, this decrease in mean drop diameters in deep convective storms is also associated with a large reduction of rainfall rate at 2.5 km associated with the AM event when compared with the PM events (not shown). This indicates that breakup and evaporation processes play a more important role in rainfall production within the AM events, while coalescence is probably more efficient within the PM events.

[47] In the mature phase (5 h before to 1 h after the peak) where increasingly higher convective cloud tops associated with deep convection are found (Figure 9c), there is a large increase in D_0 and a decrease in N_w when compared with the buildup phase. This clearly indicates that coalescence processes are more efficient in that phase than during the
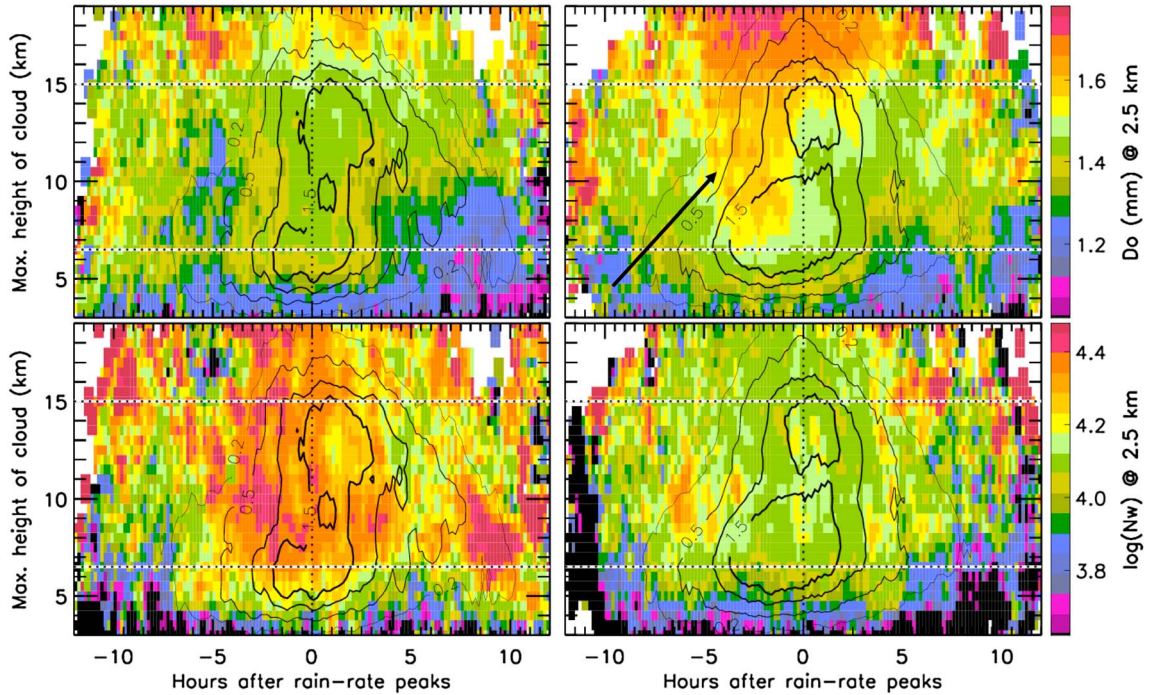
Figure 11. The same format as Figures 9d and 9e, except shows (top) D_0 and (bottom) N_w at 2.5 km associated with events in the (left) AM class and (right) PM class. The overplotted contour curves in black represent the CTH frequency as shown in Figures 9d and 9e, normalized by the number of events in each class.

buildup phase. It is striking to see how the microphysics of deep convective storms is very different in that mature phase between the AM and PM events. In the AM events, the N_w is actually increasing a lot, ~400% higher, when entering the mature phase (while it was slightly decreasing in the PM events), while the D_0 is increasing, but with a time lag with respect to the PM events similar to that observed for the increase in convective cloud top heights. Overall it is found that drops in the AM deep convective clouds are on average larger but in much smaller concentration than those in the PM deep convective clouds. In other words, deep convective rainfall characteristics in the mature stage of the life cycle of the AM and PM events are completely different.

[48] Finally, in the decay phase (from 1 h after the rainfall peak), the atmosphere returns to the same conditions as during the buildup phase for the PM events (Figure 11, right) and "all events" (not shown). It is not the case at all for the AM events, in which the rainfall parameters are very different from the buildup phase, especially for convective tops lower than 10 km, where mean drop diameters are much smaller and N_w are larger than during the buildup. This higher N_w is indicative of new convective developments. This seems to be in good agreement with larger frequencies of occurrence of cloud top heights in the 7–12 km height layer in Figure 9d as compared to Figure 9e.

5. The Temporal Evolution of the Large-Scale Moisture Budget During Rain Events

[49] In this section, we explore the evolution of large-scale moisture budget around the rainfall events identified above with the goal to better understand the relative role of

dynamical and physical processes in the transition from shallow to deep convection. Due to their structural differences, the analysis is performed separately for the morning and afternoon rainfall events defined above. Figures 12a and 12b show the time evolution of the vertically resolved budget of specific humidity for ±12 h on either side of the AM and PM events, respectively. The large-scale moisture budget is divided into four terms, namely the moisture tendency (q tend) which arises from contributions from horizontal advection (q adv h), vertical advection (q adv v), and the residual term (Q2). In summary, q tend = q adv h + q adv v + Q2. The Q2 term represents the collective effects of all subdomain-scale processes [see *Yanai et al.*, 1973]. All terms are scaled to the same units of humidity change with time, i.e., $g\,kg^{-1}\,h^{-1}$.

[50] The large-scale data set has a 6-hourly resolution, and so within the 24 h window around each rainfall event, there will be between four and five profiles. The time stamps of the large-scale data with respect to the onset time of the rain events in both the AM and PM classes are represented by the short vertical lines above the humidity tendency panels. It is clear from this illustration that due to the high time resolution (10 min) of the radar data used to define the rain events, the timing of the large-scale data entering the composite is nearly continuous around $t = 0$ h. Thus, the observed temporal evolution of the moisture budget terms in Figure 11 is robust even on an hourly scale, despite using the 6-hourly forcing data set.

[51] Considering the humidity tendency itself, it is evident that both classes of events are characterized by moistening during the storm buildup phase that gradually increases in depth from the boundary layer to the middle troposphere. For the AM events, the moistening starts earlier than for the
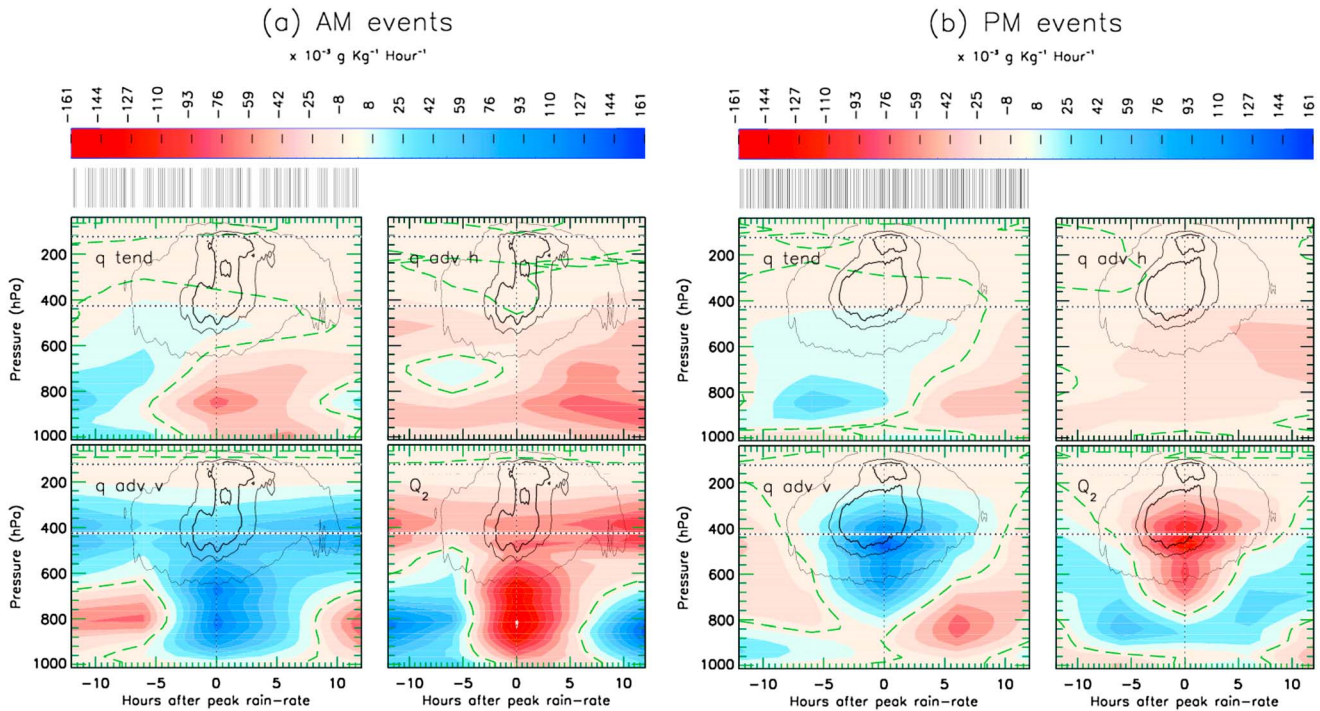
Figure 12. Superposed epoch analyses (composite) responses of Q terms for up to 12 h on either side of rain events identified to occur within (a) 00:00 A.M.–08:00 A.M. and (b) 12:00 P.M.–08:00 P.M. A bin size of 6 h in time and 50 hPa in pressure was used in this figure. The overplotted green curve shows the location of "0 amounts" in each panel, and the series of black curve is the CTH frequency as shown in Figures 9d and 9e. The vertical black lines above the humidity tendency panels indicate the large-scale profile times relative to the rainfall events used in the composite analysis.

PM events. It is often speculated that the main source of the midlevel moistening are cumulus congestus clouds. While not entirely conclusive, the breakdown of the humidity tendency into three components allows for an investigation of this hypothesis.

[52] It is evident that for both types of events, the horizontal advection terms are negative. This is understandable as areas of heavy rain are moist, making it likely that the surrounding area is drier leading to negative humidity gradients away from the rainy area. For both sets of events, it is the vertical advection term as well as the subdomain-scale terms that contribute to the midlevel moistening, albeit in quite different ways between the event types.

[53] For the AM events, which have been shown to be mostly oceanic in nature, the period from −12 to −5 h is characterized by drying of the middle troposphere (implying downward large-scale motion), compensated by moistening by subdomain processes. While it is tempting to ascribe this moistening to congestus clouds, it is evident from the evolution of the cloud characteristics (Figure 9 and replotted as grey contours in Figure 12) that no such clouds exist at this time. The fact that the atmosphere is ascending above the midlevels while the subgrid processes dry the upper troposphere makes it more likely that the middle tropospheric moistening by small-scale processes is a result of the evaporation of precipitation from stratiform clouds that are likely remnants of previous convective events. This is also consistent with a very similar evolution of the moisture budget after the main rain events (+9 h and onward). Approximately 8 h before the rainfall event, the vertical

advection term turns positive near the surface increasing in depth as time progresses, reaching its peak during the event at midlevels. This implies a profile of increasing vertical motion with height, and hence low-level convergence, and indicates that it is large-scale dynamical, not small-scale, processes that dominate the evolution from shallow to deep convection. This is consistent with the findings of *Hohenegger and Stevens* [2012].

[54] The moisture evolution for the (land-based) PM events is somewhat different. The vertical advection term is positive at low levels for the entire prerainfall period. This is likely a result of net convergence into the domain in support of the widespread sea breeze circulations developing during the day. The moistening from this term is weak and increases in height a few hours before the main rainfall event. There is a distinct peak in moistening from small-scale processes approximately 5 h before the main rainfall event at 800 hPa, accompanied by the drying of the levels below, indicative of the presence of nonprecipitating shallow cumulus clouds. As is evident from the overlaid radar CTH evolution, the bulk of the congestus clouds appears after this peak and is not directly associated with it. In fact, the moistening by small-scale processes weakens when the congestus clouds appear, making it unlikely that they play a major role in setting the conditions for deep convection. More likely, they constitute a transitional stage of convection as the large-scale atmosphere transits from suppressed (−12 to −5 h) to convectively active (−5 to +5 h) conditions. The latter are characterized by a very strong compensation in the humidity tendency between large-scale dynamical

processes (moistening) and small-scale convective processes (drying), indicating the very strongly dynamically coupled nature of precipitating deep convection.

6. Conclusion and Summary

[55] Wet season (October–April) C-band polarimetric (CPOL) radar observations of cumulus cloud top heights (CTHs) and their rainfall properties over a 3 year period (2004–2007) at the Darwin site have been used to objectively identify different tropical cumulus modes. Once these cumulus modes were established, the study then focused on studying the progression of the different modes around several carefully selected heavy rainfall events by using a composite analysis applied separately to events experienced in morning (oceanic) and afternoon (continental) conditions. The large-scale moisture budget was analyzed to reveal the relative role of dynamical and physical processes in the transition from shallow to deep convection during the rainfall events.

[56] The study first showed that the CPOL radar is capable of observing cumulus congestus mode (aka, Mode 2) but misses most of the shallow cumulus mode (aka, Mode 1). This was verified by comparing the CTH statistics from CPOL with concurrent observations from a millimeter-wavelength cloud radar (MMCR). In deeper convection (aka, Modes 3 and 4), the CPOL performance was shown to be better than that of the MMCR, as expected.

[57] The identification and further study of individual cumulus cloud cells revealed that the cell rainfall properties at 2.5 km height change remarkably with CTH. This allowed an objective way of identifying four different cloud types: a shallow cumulus mode with CTH in the trade inversion layer (1–3 km), a congestus mode with tops in the highly stable middle troposphere (3–6.5 km), a deep convective mode with tops in the region of free convection (6.5–15 km), and an overshooting convection mode with tops in the tropical tropopause layer (CTH > 15 km). The four CTH layers of the cumulus modes are also visible in temperature lapse rates. Furthermore, the vertical profile of the reflectivity lapse rates is also found to contrast strongly between the different cumulus cloud modes.

[58] The study then examined the temporal evolution of the identified cumulus modes during heavy rainfall events. Overall, the daily rainfall pattern in the Darwin region is semidiurnal in nature, with the larger afternoon peak clearly associated with continental-based convection and the secondary peak associated with oceanic convection. The two types of events were studied separately by considering events between 00:00 A.M. and 08:00 A.M. local time (AM class with 39 events) and 12:00 P.M.–08:00 P.M. local time (PM class with 78 events). In both sets of events, there is a distinct evolution of cloud top height involving a "congestus" phase that starts 5–8 h before the rainfall peak. The deeper modes begin to form shortly before the onset time of rainfall events. All cumulus modes decay nearly at the same time, approximately 3 h after the rainfall peak. For the oceanic AM events, the ratio of the shallow to the deep population is higher and the transition time from the shallow to the onset of deep population is shorter than for the continental PM events. The convective-scale microphysical properties, represented by retrieved mean drop diameter D_0 and drop concentration N_w, were found to be very different between the two rain event classes. This indicates that different microphysical processes dominate over different underlying surfaces during convective storms.

[59] A composite analysis of the large-scale moisture budget during the rainfall events implies that for both the AM and PM events, the moistening peaks before the peak in the congestus population. In both sets of events, large-scale dynamical processes play a significant role in the transition from shallow to deep clouds. This leads to the conclusion that the transition to deep convection is characterized by a close interplay between a moistening of the middle troposphere by congestus clouds and the heating-induced convergence on larger scales.

[60] Many more studies of this kind using a combination of instruments such as merged cloud radar, CPOL, and in situ observations, and over different underlying surface conditions such as oceanic and continental are needed to further understand the rainfall properties of the four cumulus cloud modes identified here and their evolution during rainfall events. In particular, the shallow cumulus mode (Mode 1), its rainfall properties and role, if any, in increasing the congestus formation (Mode 2) and subsequent deep clouds (Modes 3 and 4) needs to be investigated with more suitable scanning radars and higher resolution space-time observation of the atmospheric moisture and thermal gradients. Also, it would be worthwhile to analyze the tropical data with strategies developed in studies already undertaken at midlatitudes [e.g., *Zhang and Klein*, 2010].

References

Ackerman, T. A., and G. M. Stokes (2003), The atmospheric radiation measurement program, *Phys. Today*, *56*, 38–45.

Bringi, V. N., C. R. Williams, M. Thurai, and P. T. May (2009), Using dual-polarized radar and dual-frequency profiler for DSD characterization: A case study from Darwin, Australia, *J. Atmos. Oceanic Tech.*, *26*, 2107–2122.

Casey, S. P. F., E. J. Fetzer, and B. H. Kahn (2012), Revised identification of tropical oceanic cumulus congestus as viewed by CloudSat, *Atmos. Chem. Phys.*, *12*, 1587–1595.

Chen, Y., and A. D. Del Genio (2009), Evaluation of tropical cloud regimes in observations and a general circulation model, *Climate Dynam.*, *32*, 355–369.

Del Genio, A. D., Y.-H. Chen, D. Kim, and M.-S. Yao (2012), The MJO transition from shallow to deep convection in CloudSat/CALIPSO data and GISS GCM simulations, *J. Climate*, *25*, 3755–3770, doi:10.1175/JCLI-D-11-00384.1.

Hohenegger, C., and B. Stevens (2012), Preconditioning deep convection with cumulus congestus, *J. Atmos. Sci.*, *70*, 448–464, doi:10.1175/JAS-D-12-089.1.

Houze, R. A., and C.-P. Cheng (1977), Radar characteristics of tropical convection observed during GATE: Mean properties and trends over the summer season, *Mon. Weather Rev.*, *105*, 964–980.

Jakob, C. (2010), Accelerating progress in global atmospheric model development through improved parameterizations: Challenges, opportunities and strategies, *Bull. Am. Meteorol. Soc.*, *91*, 869–875.

Jakob, C., L. Davies, V. V. Kumar, and P. T. May (2011), Representing convection in models—How stochastic does it need to be?, *Proceedings of the ECMWF Workshop on "Representing Model Uncertainty and Error in Weather and Climate Prediction"*, ECMWF.

Jensen, M. P., and A. D. Del Genio (2006), Factors limiting convective cloud-top height at the ARM Nauru Island climate research facility, *J. Climate*, *19*, 2105–2117.

Johnson, R. H., T. M. Rickenbach, S. A. Rutledge, P. E. Ciesielski, and W. H. Schubert (1999), Trimodal characteristics of tropical convection, *J. Climate*, *12*, 2397–2418.

Keenan, T. D., K. Glasson, F. Cummings, T. S. Bird, J. Keeler, and J. Lutz (1998), The BMRC/NCAR C-band polarimetric (CPOL) radar system, *J. Atmos. Oceanic Tech.*, *15*, 871–886.

Kemball-Cook, S. R., and B. C. Weare (2001), The onset of convection in the Madden-Julian oscillation, *J. Climate*, *14*, 780–793.

Kikuchi, K., and Y. N. Takayabu (2004), The development of organized convection associated with the MJO during TOGA COARE IOP: Trimodal characteristics, *Geophys. Res. Lett.*, *31*, L10101, doi:10.1029/2004GL019601.

Kingsmill, D. E., and R. M. Wakimoto (1991), Kinematic, dynamic, and thermodynamic analysis of a weakly sheared severe thunderstorm over northern Alabama, *Mon. Weather Rev.*, *119*, 262–297.

Kuang, Z., and C. S. Bretherton (2006), A mass-flux scheme view of a high-resolution simulation of a transition from shallow to deep cumulus convection, *J. Atmos. Sci.*, *63*, 1895–1909.

Kumar, V. V., A. Protat, P. T. May, C. Jacob, G. Penide, S. Kumar, and L. Davies (2013), On the effects of large-scale environment and surface conditions on convective cloud characteristics over Darwin, Australia, *Mon. Weather Rev.*, doi:10.1175/MWR-D-12-00160.1.

Kumar V. V., and V. Ramachandran (2004), Rain-attenuation measurement at 11.6 GHz in Suva, Fiji, *Electron. Lett*, Institution of Electrical Engineers, United Kingdom, *40*(22), 1429–1431.

Lin, X., and R. H. Johnson (1996), Heating, moistening, and rainfall over the western Pacific warm pool during TOGA COARE, *J. Atmos. Sci.*, *53*, 3367–3383.

Liu, C., and E. J. Zipser (2008), Diurnal cycles of precipitation, clouds, and lightning in the tropics from 9 years of TRMM observations, *Geophys. Res. Lett.*, *35*, L04819, doi:10.1029/2007GL032437.

Malkus, J. S., and H. Riehl (1964), *Cloud Structure and Distributions Over the Tropical Pacific Ocean*, pp. 229, University of California Press, London, England.

Mapes, B. E., S. Tulich, J. Lin, and P. Zuidema (2006), The mesoscale convection life cycle: Building block or prototype for large-scale tropical waves?, *Dyn. Atmos. Oceans*, *42*, 3–29.

May, P. T., C. Long, and A. Protat (2012), The diurnal cycle of the boundary layer, convection, clouds, and surface radiation in a coastal monsoon environment (Darwin Australia), *J. Climate*, *25*, 5309–5326, doi:10.1175/JCLI-D-11-00538.1.

May, P. T., and A. Ballinger (2007), The statistical characteristics of convective cells in a monsoon regime (Darwin, Northern Australia), *Mon. Weather Rev.*, *138*, 55–73.

May, P. T., J. H. Mather, G. Vaughan, C. Jacob, G. M. McFarquhXar, K. N. Bower, and G. G. Mace (2008), The Tropical Warm Pool International Cloud Experiment, *Bull. Am. Meteorol. Soc.*, *89*, 629–645.

Melnikov, V. M., D. S. Zrnić, R. J. Doviak, P. B. Chilson, D. B. Mechem, and Y. Kogan (2011), Prospects of the WSR-88D radar for cloud studies, *J. Appl. Meteorol. Climatol.*, *50*, 859–872.

Miller, M. A., J. Verlinde, C. V. Gilbert, G. J. Lehenbauer, J. S. Tongue, and E. E. Clothiaux (1998), Detection of nonprecipitating clouds with the WSR-88D: A theoretical and experimental survey of capabilities and limitations, *Wea. Forecasting*, *13*, 1046–1062.

Moran, K. P., B. E. Martner, M. J. Post, R. A. Kropfli, D. C. Welsh, and K. P. Widener (1998), An unattended cloud-profiling radar for use in climate research, *Bull. Am. Meteorol. Soc.*, *79*, 443–455.

Penide, G., V. V. Kumar, A. Protat, and P. T. May (2013), Statistics of drop size distribution parameters and rain rates for stratiform and convective precipitation during the North Australian wet season, *Mon. Weather Rev.*, doi:10.1175/MWR-D-12-00262.1.

Pope, M., C. Jakob, and M. Reeder (2009a), Regimes of the North Australian wet season, *J. Climate*, *22*, 6699–6715.

Pope, M., C. Jakob, and M. Reeder (2009b), Objective classification of tropical mesoscale convective systems, *J. Climate*, *22*, 5797–5808.

Redelsperger, J. -L., D. B. Parsons, and F. Guichard (2002), Recovery processes and factors limiting cloud-top height following the arrival of a dry intrusion observed during TOGA COARE, *J. Atmos. Sci.*, *59*, 2438–2457.

Rickenbach, T. M., and S. A. Rutledge (1998), Convection in TOGA COARE: Horizontal scale, morphology, and rainfall production, *J. Atmos. Sci.*, *55*, 2715–2729.

Schafer, R., P. T. May, T. D. Keenan, K. McGuffie, W. L. Ecklund, P. E. Johnston, and K. S. Gage (2001), Boundary layer development over a tropical island during the Maritime Continent Thunderstorm Experiment, *J. Atmos. Sci.*, *58*, 2163–2179.

Sherwood, S. C., and R. Wahrlich (1999), Observed evolution of tropical deep convective events and their environment, *Mon. Weather Rev.*, *127*, 1777–1795.

Simpson, J., T. D. Keenan, B. Ferrier, R. H. Simpson, and G. J. Holland (1993), Cumulus mergers in the maritime continent region, *Meteorol. Atmos. Phys.*, *51*, 73–99.

Steiner, M., R. A. Houze Jr., and S. E. Yuter (1995), Climatological characterization of three-dimensional storm structure from operational radar and rain gauge data, *J. Appl. Meteorol.*, *34*, 1978–2007.

Stokes, G. M., and S. E. Schwartz (1994), The Atmospheric Radiation Measurement (ARM) Program: Programmatic background and design of the cloud and radiation testbed, *Bull. Am. Meteorol. Soc.*, *75*, 1201–1221.

Testud, J., S. Oury, P. Amayenc, and R. A. Black (2001), The concept of "normalized" distributions to describe raindrop spectra: A tool for cloud physics and cloud remote sensing, *J. Appl. Meteorol.*, *40*, 1118–1140.

Tromeur, E., and W. B. Rossow (2010), Interaction of tropical deep convection with the large-scale circulation in the MJO, *J. Climate*, *23*, 1837–1853.

Waite, M. L., and B. Khouider (2010), The deepening of tropical convection by congestus preconditioning, *J. Atmos. Sci.*, *67*, 2601–2615.

Xie, S., R. T. Cederwall, and M. Zhang (2004), Developing long-term single-column model/cloud system—Resolving model forcing data using numerical weather prediction products constrained by surface and top of the atmosphere observations, *J. Geophys. Res.*, *109*, D01104, doi:10.1029/2003JD004045.

Xie, S., T. Hume, C. Jacob, S. A. Klein, R. McCoy, and M. Zhang (2010), Observed large-scale structures and diabatic heating and drying profiles during TWP-ICE, *J. Climate*, *23*, 57–79.

Yanai, M., S. Esbensen, and J. Chu (1973), Determination of bulk properties of tropical cloud clusters from large-scale heat and moisture budgets, *J. Atmos. Sci.*, *30*, 611–627.

Zhang, M., and J. Lin (1997), Constrained variational analysis of sounding data based on column-integrated budgets of mass, heat, moisture, and momentum: Approach and application to ARM measurements, *J. Atmos. Sci.*, *54*(11), 1503–1524.

Zhang, Y., and S. A. Klein (2010), Mechanisms affecting the transition from shallow to deep convection over land: Inferences from observations of the diurnal cycle collected at the ARM Southern Great Plains site, *J. Atmos. Sci.*, *67*, doi:10.1175/2010JAS3366.1.

Zipser, E. J., and K. R. Lutz (1994), The vertical profile of radar reflectivity of convective cells: A strong indicator of storm intensity and lightning probability?, *Mon. Weather Rev.*, *122*, 1751–1759.

Zrnić, D. S., and A. V. Ryzhkov (1998), Polarimetry for weather surveillance radars, *Bull. Am. Meteorol. Soc.*, *80*(3), 389–406.